ACS ES&T Air

Open Access

pubs.acs.org/estair

Article

When Size Matters: Size-Selective Chemistry in the Heterogeneous Processing of Organic Aerosols

Published as part of ACS ES&T Air special issue "John H. Seinfeld Festschrift".

Marcel Douverne and Thorsten Hoffmann*

Cite This: *ACS EST Air* 2025, 2, 2491−2503

Read Online

ACCESS | Metrics & More | Article Recommendations | Supporting Information

ABSTRACT: New particle formation and growth in the atmosphere critically influence cloud properties and climate, as well as human health through the presence of ultrafine particles. While the early stages of particle nucleation are increasingly understood, the mechanisms driving the subsequent growth of nanoparticles, particularly the role of organic compounds, remain unclear. This study investigates the heterogeneous ozonolysis of 5-norbornene-2-endo,3-exodicarboxylic acid (NDA) in size-selected aerosol particles (30−110 nm) under varying relative humidity and ozone conditions. NDA serves as a model compound representative of unsaturated monoterpene derivatives with low volatility and high particle-phase partitioning. Using real-time mass spectrometry, we explore how particle size influences both reactivity and product distribution. Our results reveal pronounced particle-size and humidity dependencies: smaller particles favor dimerization and oligomer formation, likely due to increased Laplace pressure, whereas larger particles promote hydrolysis and decomposition reactions. The findings suggest that nanometer-sized particles provide a distinct chemical microenvironment that alters the course of multiphase reactions, thereby affecting particle aging, volatility, and growth potential. These results underscore the importance of considering particle-size-dependent chemistry in models of atmospheric aerosol formation and evolution.

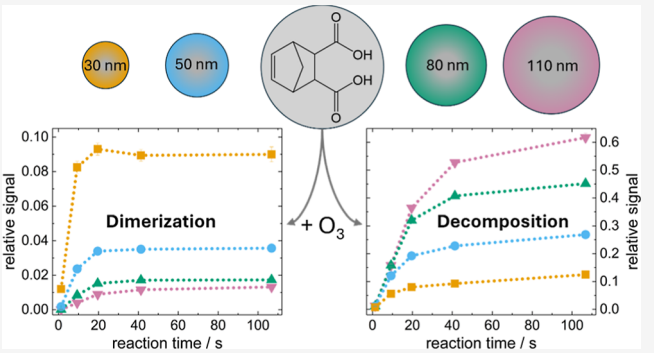

KEYWORDS: *particle-size-dependent chemistry, heterogeneous ozonolysis, size-selected aerosol nanoparticles, relative humidity effects, multiphase reactions, particle aging, laplace pressure, chemical ionization mass spectrometry (CIMS), particle evaporation*

INTRODUCTION

The formation of new particles in the atmosphere is the source of about half of cloud condensation nuclei (CCN) and thus influences the properties of clouds and the Earth's energy balance.[1−4] Ultrafine particles in the atmosphere (<100 nm) also pose a health risk because they can penetrate deep into the respiratory tract.[5] Although new insights into the chemical compounds involved in the initial stages of particle formation have been obtained in recent years,[6,7] there are still considerable gaps in our knowledge regarding the growth processes of nanoparticles.[8−10] An open question is which substances drive the further growth of particles in the nanometer range after the formation of the first molecular clusters. Although it is generally accepted that organics make the greatest contribution during this growth phase, it is not known which compounds and through which mechanism the organic substances actually contribute. Since sufficiently low volatility is a necessary prerequisite, potential candidate molecules must either be highly oxidized multifunctional products (so-called HOMs) or have higher molecular weights formed by accretion reactions of ubiquitous smaller molecular units (oligomerization).[11−15] Today, the nucleation process is mainly discussed on the basis of the first pathway, the formation of low-volatile substances from oxidation reactions in the gas phase with additional functional groups and their phase transition through condensation.[16] However, evidence also suggests that accretion reactions, in which SOA components combine to form higher-molecular-weight products, occur in the particle phase. This provides a pathway for the formation of extremely low-volatility compounds.[17−19] If particle-phase chemistry is size-dependent (i.e., more favorable in smaller particles), this process could be particularly important, as it may critically affect the balance between survival and loss of freshly formed particles. Such reactions could enhance particle growth and help counteract the

Received: May 19, 2025
Revised: September 24, 2025
Accepted: September 25, 2025
Published: October 2, 2025

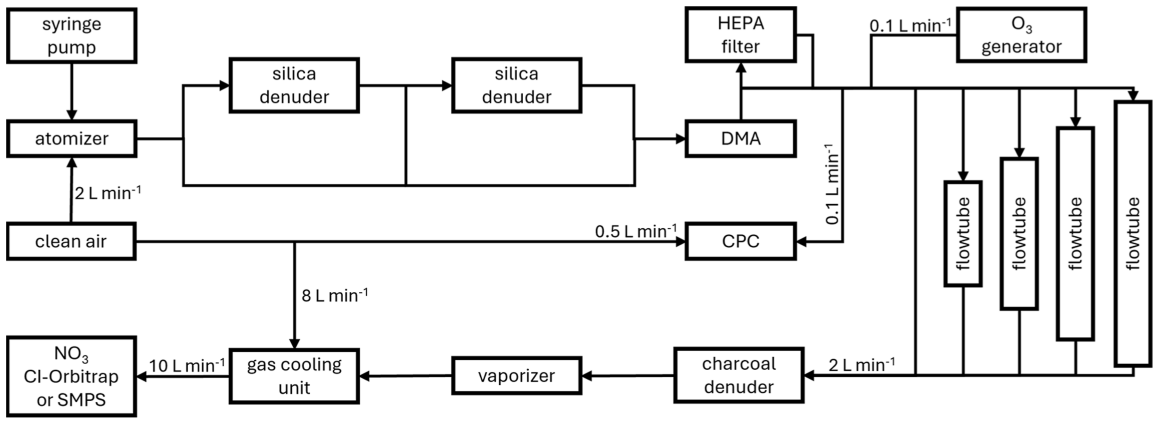

Figure 1. Schematic of the experimental setup. The SMPS was used as the detection system only in experiments dedicated to determining particle evaporation efficiency. In the experiments listed in Table 2, the CI-Orbitrap served as the detection system.

tendency of small particles to be lost through Brownian coagulation. Size-dependent particle-phase chemistry may even proceed more rapidly than gas-phase pathways that generate low-volatility compounds.[20]

An obvious difference in the properties of aerosol particles that is strongly dependent on particle size is the surface-to-volume ratio. In particular for heterogeneous reactions, when one of the reaction partners from the gas phase comes into contact with reaction partners in the particle phase, as is the case in the heterogeneous ozonolysis of particle-bound olefins carried out here, smaller particles with a correspondingly larger surface area result in an increased conversion at the same mass concentration. However, it is more interesting to ask whether there are other size-dependent differences besides the purely geometric ratio of surface area to volume, especially those that can influence product formation itself (i.e., resulting in different products in particles of different sizes). In connection with aqueous aerosols, special properties of the air−water interface have been discussed recently. For example, molecular dynamics simulations suggest that although the pH value in aqueous aerosol particles is uniform on average (i.e., not size-dependent), the hydronium and hydroxide ions within a particle exhibit significant concentration gradients which extend from the outer molecular layers to the interior of the particles, with the interface being enriched with hydronium cations and depleted with hydroxide anions.[21] In small aqueous aerosol particles in particular, this leads to different conditions prevailing inside the particles than in the surface layers. In fact, there have been a number of recent studies in this field of research dealing with nano- and microdroplets, which focus on the question of whether chemical reactions proceed differently here than in a homogeneous phase.[22,23] In particular, the massive influence on a number of redox reactions has attracted considerable attention and is currently being discussed from various perspectives.[24−26]

In addition to the current discussions on size- or curvature-dependent reactivity of aqueous aerosols, there are undoubtedly other particle size-dependent phenomena that may be directly related to chemical reactions in the particle phase, such as the viscosity of aerosol particles, which can have a direct influence on the course of reactions, particularly in heterogeneous chemical processes.[27] Another strongly size-dependent phenomenon is the rise in internal pressure, known as Laplace pressure, as particle diameter decreases.[28] This pressure difference between the particle interior and exterior arises from the interplay of surface tension and curvature, increasing significantly with smaller radii.[29−31] Since bond-forming chemical reactions (e.g., oligomerization) are favored at higher pressures, such reactions gain importance in the smallest particles.

Real-time studies of the chemical composition of nanometer particles are challenging.[32,33] For this work, we use a self-built particle evaporator coupled to a CI-Orbitrap mass spectrometer with upstream particle size selection. As a chemical system, we investigate the heterogeneous ozonolysis of 5-norbornene-2-endo,3-exodicarboxylic acid (NDA) in aerosol particles of different sizes. NDA combines the high ring strain of a bicyclic monoterpene system, similar to α-pinene,[34] with two additional polar carboxylic acid groups, resulting in a lower vapor pressure and enhanced particle-phase partitioning. Due to its structural characteristics, NDA serves as a proxy for unsaturated monoterpene derivatives, which are known to contribute to secondary organic aerosol (SOA) formation. Although previous studies have shown that oxidized unsaturated monoterpene derivatives (e.g., limononic acid) in the condensed phase undergo further oxidation and thereby influence aerosol formation during atmospheric aging,[35,36] indicating that the reactions investigated here are also relevant to atmospheric aerosol formation, NDA was primarily chosen for this study because it serves as a suitable model compound. Specifically, NDA enables the generation of a stable aerosol population within the targeted size range (30−110 nm) and facilitates real-time investigation of the particle phase using mass spectrometry. Special emphasis is placed on how particle size influences not only the overall reactivity but also the chemical composition and evolution of the reaction products. By systematically varying particle sizes and environmental conditions (relative humidity and O_3 concentrations), we provide mechanistic insights into particle-size-dependent chemistry, contributing to a better understanding of the molecular-level processes that govern the aging of organic aerosols in the atmosphere. The purpose of this publication is to present experimental results that seek to answer the question of whether very small organic aerosol particles provide a unique chemical environment in the nanometer range that can influence the course of chemical reactions.

MATERIALS AND METHODS

Flow Tube Experiments. For particle generation, a solution was prepared using a 9:1 (v/v) mixture of deionized

https://doi.org/10.1021/acsestair.5c00189
ACS EST Air 2025, 2, 2491−2503

water (18.2 MΩ·cm) and isopropanol (>98%, Fisher Chemical) containing 540 mg L^{-1} 5-norbornene-2-endo,3-exodicarboxylic acid (NDA) (97%, Sigma-Aldrich) and 60 mg L^{-1} tricarballylic acid (TA) (98%, Alfa Aesar) as internal standard. This solution was then nebulized using a Model 3076 Constant Output Atomizer (TSI Incorporated, Shoreview, MN) with purified air (2 L min^{-1}) at a flow rate of 350 μL min^{-1} supplied by a syringe pump. The experimental setup is illustrated in Figure 1. The experiments were conducted at three different relative humidity (RH) conditions. These were adjusted by passing the aerosol either through no silica denuder (85 ± 3%), one silica denuder (50 ± 3%), or two silica denuders (35 ± 4%) after nebulization. Under these conditions, the resulting particle-size distributions peak at around 40 and 50 nm, with most particles falling within the 20−120 nm range (Figure S1). The polydisperse aerosol was subsequently size-selected using an Electrostatic Classifier Model 3082 with an Advanced Aerosol Neutralizer Model 3088 and a Nano-DMA (TSI Incorporated). Particles with diameters of 30, 50, 80, and 110 nm were investigated. The particle concentration was controlled via a valve and an inline HEPA filter. Based on the TA signal from the mass spectrometer, the volume concentration in the flow tubes was maintained nearly constant across particle sizes. The resulting particle concentration was measured using a water-based Condensation Particle Counter (CPC) Model 3789 (TSI Incorporated) operating in 2 nm mode, with an aerosol sample flow of 0.1 L min^{-1}. The remaining monodisperse aerosol flow (1.9 L min^{-1}) was mixed with 0.1 L min^{-1} ozone-containing air. Ozone was generated using a modified ozone generator (Dasibi 1008-RS) and subsequently diluted to the desired concentrations. To investigate the reaction system at different reaction times, the reaction mixture was analyzed either immediately after mixing or after passing through four different flow tubes of varying volumes under dark conditions. The dimensions of the flow tubes and the corresponding reaction times are provided in Table 1. Table 2 summarizes the experimental conditions for each experiment.

Table 1. Length and Volume of the Utilized Flow Tubes and the Corresponding Reaction Time With a Flow Rate of 2 L min^{-1}

length (cm)	volume (mL)	reaction time (s)
–	–	1.3 ± 0.5
45	264 ± 5	9.3 ± 0.7
67	610 ± 5	19.6 ± 0.7
82	1334 ± 5	41.3 ± 0.7
120	3514 ± 5	106.8 ± 0.7

Because at a given classifier voltage not only singly charged particles but also larger, multiply charged particles can pass the DMA, there is a risk that the measured signal is dominated by the latter due to their greater volume. To assess this effect, we performed tandem-DMA measurements using a butanol-based condensation particle counter (CPC, Model 5416) downstream of a long DMA (L-DMA, Model 55-U; both Grimm Aerosol Technik).[37] These measurements indicate that doubly and triply charged particles contribute only marginally (Figure S2). The cumulative particle-volume distributions show that, for all investigated set point diameters, the majority of the signal arises from particles within the target size range (Figure S3).

Table 2. Experimental Conditions for the Different Experiments[a]

experiment	$[O_3]$ (ppm)	RH (%)	particle volume ($\mu m^3 \cdot cm^{-3}$)	TA signal[b] ($\cdot 10^{-2}$)
1	10	32−35	2.7 ± 0.3	1.38 ± 0.08
2	1	32−35	2.9 ± 0.1	1.26 ± 0.03
3	0.1	35−37	2.5 ± 0.2	1.24 ± 0.07
4	10	49−51	3.1 ± 0.2	1.22 ± 0.05
5	1	48−51	3.4 ± 0.3	1.17 ± 0.04
6	0.1	50−53	3.3 ± 0.3	1.22 ± 0.08
7	10	83−86	6.9 ± 0.4	2.18 ± 0.08
8	1	83−87	6.4 ± 0.7	1.92 ± 0.08
9	0.1	83−87	6.5 ± 0.5	2.07 ± 0.07

[a]In each experiment, particles with diameters of 30, 50, 80, and 110 nm were examined at the reaction times listed in Table 1. [b]Normalized to the reagent-ion signal.

Particle Evaporation. After the flow tubes the aerosol was first passed through an activated carbon denuder to remove the gas-phase components. The aerosol particles were then evaporated in a commercially available nozzle heater cartridge (HS Heizelemente) at 285 °C. This cartridge consists of a 20 cm long stainless steel tube with an inner diameter of 8 mm, tightly wrapped with a resistive heating element. A NiCrNi thermocouple is mounted on the surface to monitor the evaporator temperature, and the tube is thermally insulated with mineral wool. The nozzle heater cartridge is controlled by a W-35/M temperature controller with a PID control loop, allowing precise temperature adjustments in the range of 50−400 °C. At the applied flow rate of 2 L min^{-1}, the residence time of the particles in the evaporator is 0.3 s. The completeness of evaporation was assessed in a separate experiment using a butanol-based Condensation Particle Counter (CPC) Model 5416 with a preceding L-DMA Model 55-U (both Grimm Aerosol Technik). For this purpose, the evaporator temperature was varied between 25 and 325 °C, and the resulting particle-size distributions were measured. It has been shown that thermal decomposition reactions (primarily dehydration and decarboxylation) in other thermal aerosol evaporators can lead to measurement artifacts.[38,39] In our inlet, the short residence time and the use of a cooling-gas unit reduce such effects. To test this, several organic polyacids were nebulized at identical conditions and evaporated at 285 °C and the fractions of decomposition products determined (Table S1). For all acids investigated, the fraction of dehydration products was <4%, substantially lower than for other thermal aerosol evaporators.[39] The influence of thermal decomposition is therefore expected to be minor under our conditions.

CI-Orbitrap Measurements. The ion source of the CI-Orbitrap used in this study is an Eisele type CI-inlet modified for a high-resolution Orbitrap mass spectrometer.[40,41] The mass spectrometer used is a high-resolution Q-Exactive Orbitrap and HNO_3 was used as reagent gas. Initially, the particle evaporator was directly connected to the CI-Orbitrap. However, even at low evaporator temperatures below 100 °C, a significant decrease in both reagent gas and analyte signal was observed. A possible explanation for this could be the formation of turbulence within the ionization source, as Eisele-type inlets are known to be highly sensitive to flow changes.[42] To address this issue, a gas cooling unit was developed and placed between the evaporator and the CI-

https://doi.org/10.1021/acsestair.5c00189
ACS EST Air 2025, 2, 2491−2503

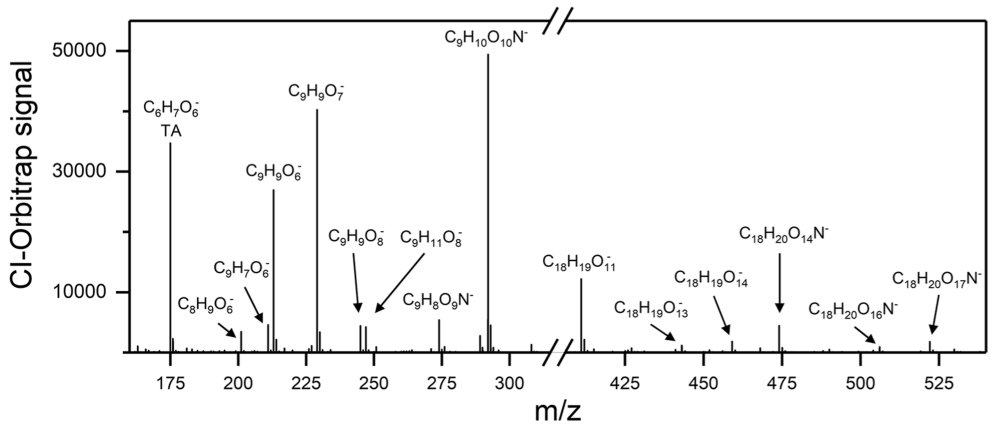

Figure 2. CI-Orbitrap mass spectra for the ozonolysis of NDA using nitrate as reagent gas. Molecular formulas of the most intense signals are indicated. For comparisons at the product level, we sum the intensities of the nitrate adducts and deprotonated ions that have the same elemental composition and then refer to the corresponding neutral species throughout. For example, the two dominant peaks ($C_9H_{10}O_{10}N^-$ (nitrate adduct); $C_9H_9O_7^-$ (deprotonated ion)) both originate from the same neutral species, $C_9H_{10}O_7$.

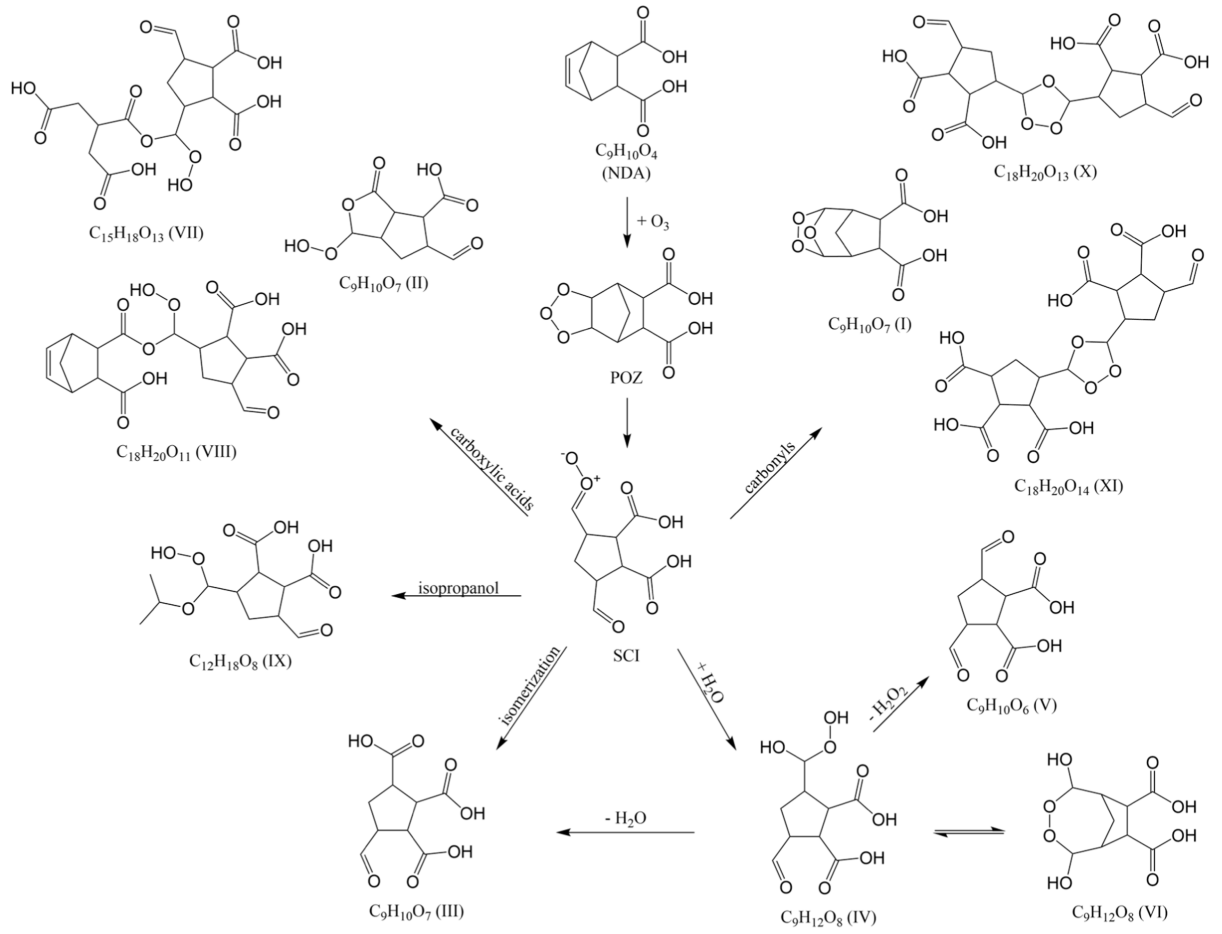

Figure 3. Proposed reaction pathways for the ozonolysis of NDA and the subsequent reactions of the SCI to form first generation oxidation products. All molecular formulas in this figure were observed in the mass spectra; structures are assigned based on established mechanisms.

Orbitrap (Figure S4). This unit cools the hot gas in two stages. First, 8 L min^{-1} of clean air is flushed around the hot stainless steel tubing coming out of the evaporator, passively cooling it and adjusting the temperature of the cooling gas to that of the analyte gas stream. Subsequently, this cooling gas serves as a sheath gas, reducing wall losses, further cooling the gas stream through mixing, and minimizing the renucleation of the cooling analyte by dilution. Implementation of the gas cooling unit reduced the loss of reagent ion signal at 320 °C from over 90% to less than 40% (Figure S5). Data analysis was performed using Orbitool, a program specifically developed for the analysis of online Orbitrap data.[43]

RESULTS AND DISCUSSION

Characterization of Reaction Products. Typical for the ozonolysis of unsaturated compounds, the reaction of NDA

https://doi.org/10.1021/acsestair.5c00189
ACS EST Air 2025, 2, 2491−2503

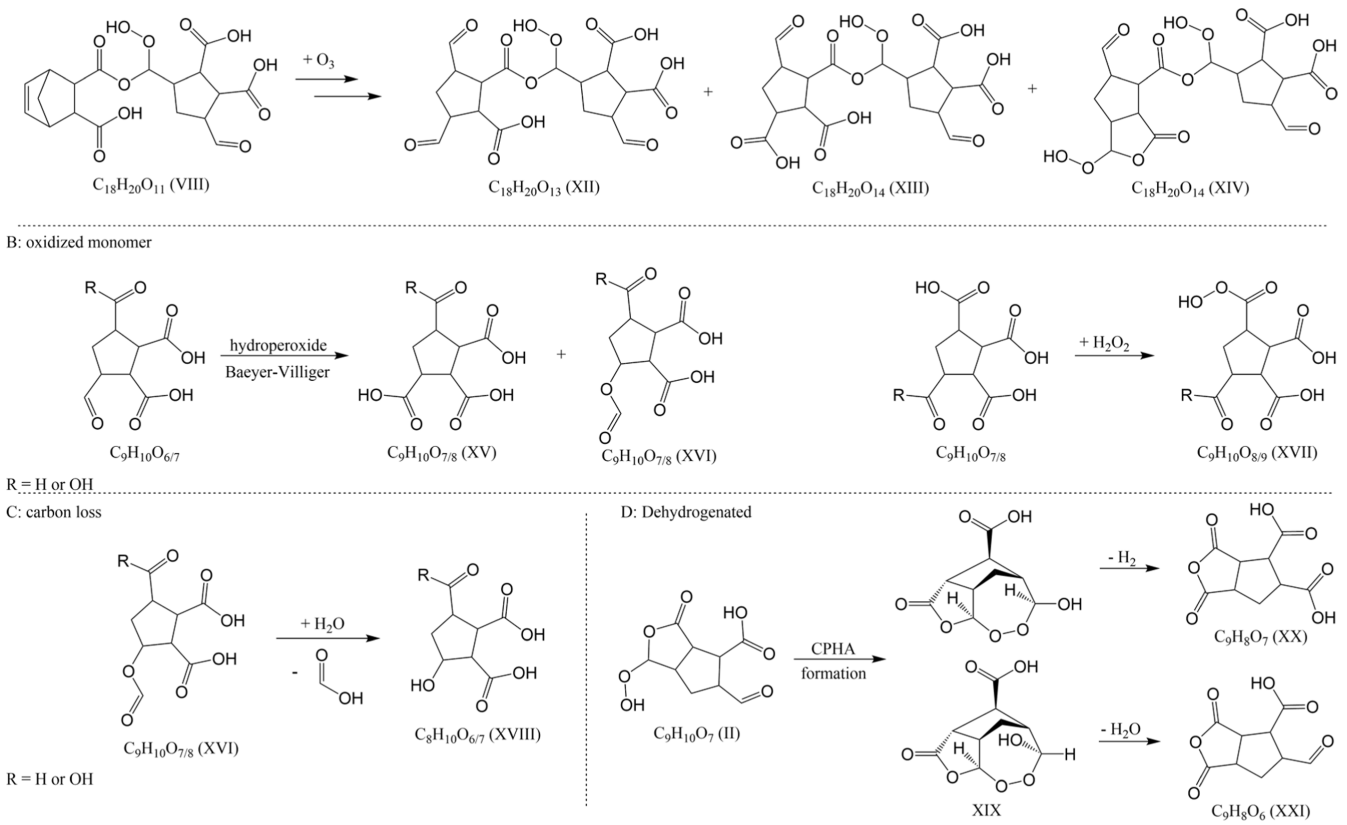

Figure 4. Proposed particle-phase reactions that lead to (A) oxidized dimers, (B) oxidized monomers, (C) carbon loss products and (D) dehydrogenated products. All molecular formulas in this figure were observed in the mass spectra; structures are assigned based on established mechanisms.

with ozone produces a wide range of products. Figure 2 shows a typical mass spectrum in negative ion mode recorded in this study using the CI-Orbitrap. Due to the high resolution of the Orbitrap, the elemental composition of the detected m/z can be directly assigned. The products are detected either as NO_3^- adducts or as deprotonated ions. For simplicity, the products are referred to as neutral species throughout this study. The signals of nitrate adducts and deprotonated species with the same elemental composition are summed, where applicable, and considered as a single products.

Similar to other unsaturated compounds, the reaction of NDA with ozone is expected to follow the Criegee mechanism (Figure 3).[44,45] We therefore attempt to derive the structures corresponding to the detected molecular formulas based on established reaction pathways of comparable unsaturated hydrocarbons. The neutral losses observed in the MS/MS measurements for the various reaction products further support the proposed structural assignments (Figures S6 and S7). The stabilized Criegee intermediate (SCI) formed in this process can undergo various reaction pathways, leading to the formation of a diverse set of product molecules. The two most intense product signals correspond to the elemental compositions $C_9H_{10}O_6$ and $C_9H_{10}O_7$, with the latter typically accounting for 50% of the signal attributed to NDA-ozonolysis products. Since NDA has the molecular formula $C_9H_{10}O_4$, these products formally represent molecules in which two or three oxygen atoms have been added to the NDA structure. The molecular formula $C_9H_{10}O_7$ probably corresponds to multiple structural isomers, including a secondary ozonide (SOZ) (I) or an α-acyloxyalkyl hydroperoxide (AAHP) (II) formed via an intramolecular reaction with one of NDA's carboxylic acid groups.[45−47] However, it could also represent a tricarboxylic acid (III), formed through isomerization of the SCI. The reaction of SCIs with water leads to the formation of α-hydroxyalkyl hydroperoxides (HAHP) which would in our case correspond to the molecular formula $C_9H_{12}O_8$ (IV).[35,47,48] HAHPs decompose by elimination of H_2O or H_2O_2.[49,50] The latter would lead to the formation of the dialdehyde $C_9H_{10}O_6$ (V). Alternatively, HAHPs can isomerize to yield a cyclic peroxyhemiacetal (VI).[51,52] In addition to these unimolecular products, signals from bimolecular reactions forming several first generation dimers are also observed. AAHPs can also form through the reaction of the SCI with carboxylic acid groups of other molecules. This would lead to the formation of $C_{15}H_{18}O_{13}$ (VII) from the reaction with the internal standard TA and $C_{18}H_{20}O_{11}$ (VIII) from the reaction with NDA. Similarly, an α-alkoxyalkyl hydroperoxide $C_{12}H_{18}O_{18}$ (IX) is produced via the reaction of the hydroxy group of isopropanol, which is added to the nebulized solution to increase particle number concentration, with the SCI.

In addition to these first-generation products, a series of m/z signals observed in the mass spectrum are likely to originate from subsequent reactions. The possible formation pathways of these compounds are depicted in Figure 4. $C_{18}H_{20}O_{13}$ and $C_{18}H_{20}O_{14}$ are probably aged dimers formed through the reaction of the unreacted double bond of the bimolecular AAHP $C_{18}H_{20}O_{11}$ (VIII) with ozone, initially generating a new SCI.[47] Similar to the monomeric SCI, this dimeric SCI can react to form an aldehyde (XII), a carboxylic acid (XIII), or an

https://doi.org/10.1021/acsestair.5c00189
ACS EST Air 2025, 2, 2491−2503

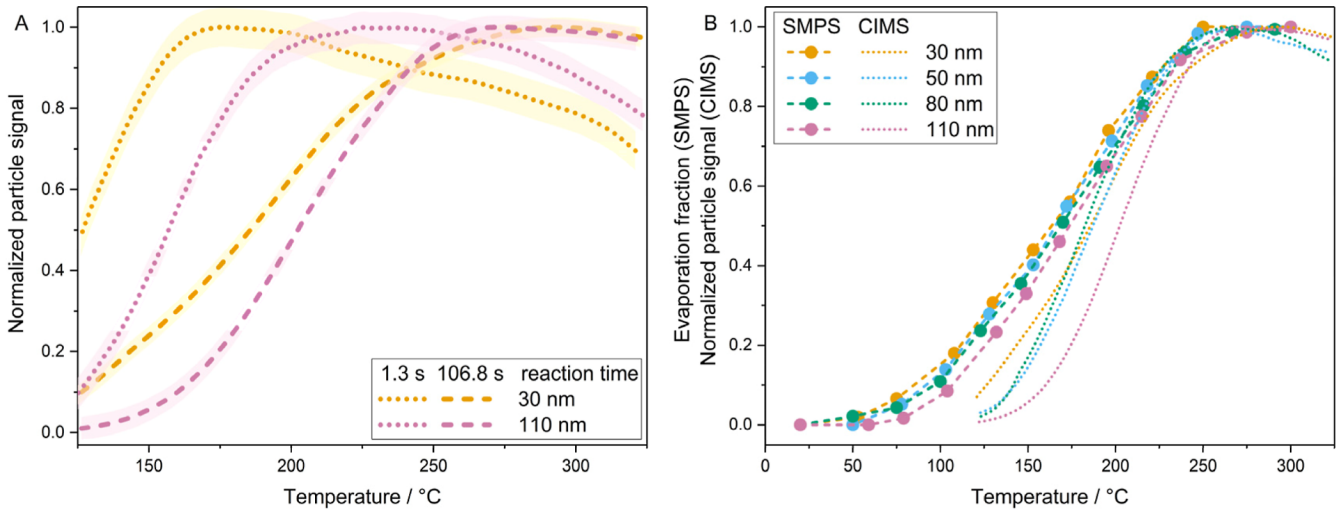

Figure 5. Adjacent-averaged thermograms of 30 nm (yellow) and 110 nm (pink) particles recorded with the CI-Orbitrap after 1.3 s (dotted lines) and 106.8 s (dashed lines) of ozonolysis time at 50% RH and 10 ppm of O_3 concentration. The semitransparent, broader band plotted behind the thermogramms denotes ±1 standard deviation (A). Comparison of adjacent-averaged thermograms recorded with the CI-Orbitrap (dotted lines) and the evaporation fraction calculated from SMPS data (dashed lines) each after 106.8 s reaction time for the respective particle sizes at 50% RH and 10 ppm of O_3 concentration for particles of 30, 50, 80, and 110 nm in diameter (B).

AAHP (XIV). However, alternative formation pathways for these highly oxidized dimers are also conceivable, such as the formation of a SOZ (X, XI) via the reaction of a monomeric SCI with carbonyl functionalities of $C_9H_{10}O_6$ or $C_9H_{10}O_7$.[46]

Another group of detected products has additional oxygen atoms in the molecule, including the molecular formulas $C_9H_{10}O_8$, $C_9H_{12}O_9$, and $C_{18}H_{20}O_{15}$. In the gas phase, autoxidation is the primary mechanism leading to highly oxygenated organic molecules (HOMs). This process involves isomerization of the SCI to a vinyl hydroperoxide, followed by the loss of an OH radical. The resulting carbon-centered radical can undergo oxygen addition to form a peroxy radical, which can further isomerize and incorporate additional oxygen atoms.[53] The formation of $C_9H_{10}O_8$ could proceed via this mechanism at the particle surface. Since this reaction pathway leads to the formation of OH radicals, we would expect to detect reaction products resulting from radical chemistry. In particular, products from the reaction of TA with OH radicals should be readily identifiable.[46] However, no such reaction products from the interaction of TA with OH radicals were observed. The MS/MS spectrum of $C_9H_{10}O_8$ shows the neutral loss of H_2O_2 (Figure S7), suggesting that it could be a hydroperoxide resulting from the reaction with oxygen. Another potential pathway for the formation of highly oxidized aged products involves reactions with hydrogen peroxide or hydroperoxide species formed during ozonolysis. H_2O_2 is known to oxidize carboxylic acids to peroxy acids.[54] $C_9H_{10}O_8$ may therefore represent a corresponding peroxy acid (XVII) formed via the reaction of $C_9H_{10}O_7$ (III) with H_2O_2. Additionally, both H_2O_2 and hydroperoxide compounds can react with aldehydes via a Baeyer−Villiger oxidation. This reaction has been suggested to play a role in SOA particle-phase chemistry and may contribute to the aging of oxidation products within particles.[55,56] H_2O_2 is released through the reaction of the SCI with water and should therefore be present in the particle phase along with various hydroperoxide species. Zhao et al. demonstrated through comparison with a reference standard that 4-cyclohexene-1,2-dicarboxylic acid undergoes oxidation to the corresponding tetraacid in a heterogeneous ozonolysis reaction, with peroxide-mediated oxidation being the most likely pathway.[46] Although the formation of carboxylic acids from aldehydes is often emphasized as the principal outcome of Baeyer−Villiger chemistry, the product distribution is shown to depend strongly on the oxidant, the solvent, and the substrate structure.[57−59] Baeyer−Villiger oxidations of terpenoid aldehydes have been reported to produce formate ester in yields of 80−90%.[60] Lehtinen et al. and Marteau et al. demonstrated that substitution at the α-carbon significantly increases the likelihood of formate ester formation, with bulkier substituents enhancing this effect.[57,61] It is therefore plausible that the ozonolysis product $C_9H_{10}O_8$ could also correspond to the tetraacid(XV) and the formate ester (XVI). This being the case would further suggest that a portion of the $C_9H_{10}O_7$ signal probably also results from the Baeyer−Villiger oxidation of one of the aldehyde groups of $C_9H_{10}O_6$ (V).

Another group of signals in the mass spectrum exhibits a loss of carbon in their molecular formula. The most prominent representatives are $C_8H_{10}O_6$ and $C_8H_{10}O_7$. We propose that these compounds could be formed through the hydrolysis of the formate esters (XVI) generated via the Baeyer−Villiger reaction.[56] This pathway would lead to the formation of alcohols (XVIII) and formic acid. Formate esters exhibit high carbonyl reactivity due to the absence of an alkyl group, making them highly susceptible to a nucleophilic attack by H_2O or other nucleophiles. Therefore, rapid hydrolysis of these esters in the aqueous particle phase would not be unlikely.

The final group of detected products is characterized by a reduced amount of hydrogen in their molecular formula. This could be explained by the elimination of molecular hydrogen or water from the molecule. The main product in this category is $C_9H_7O_6$, which could be an anhydride. Since the precursor molecule, NDA, already contains two carboxyl groups, anhydride formation could, in principle, occur prior to ozonolysis. However, due to the steric hindrance of the bicyclic structure and the fact that the two carboxyl groups are positioned in endo and exo conformations, this scenario appears unlikely. It is therefore more plausible that a carboxyl

https://doi.org/10.1021/acsestair.5c00189
ACS EST Air 2025, 2, 2491−2503

group formed during the ozonolysis process contributes to the formation. Several potential reaction pathways could lead to the formation of such an anhydride. Durham et al. demonstrated that hydroperoxides can react with aldehydes to form peroxyhemiacetals, which may decompose with the elimination of either molecular hydrogen or water.[62] It has already been proposed that this type of reaction could also occur in aerosol particles.[55,63] In our system, such a transformation could proceed via an intramolecular pathway, resulting in the formation of a cyclic peroxyhemiacetal (XIX). These cyclic intermediates are believed to decompose more rapidly than their acyclic counterparts.[64] The decomposition of a cyclic peroxyhemiacetal could, depending on the elimination step, yield either an anhydride and an aldehyde (XXI) if H_2O is eliminated, or an anhydride and a carboxylic acid (XX) if molecular hydrogen is eliminated. A bimolecular variant of this reaction, involving a hydroperoxide and a carbonyl compound forming an acyclic peroxyhemiacetal, is also conceivable, although it is likely to proceed more slowly, as mentioned above. An alternative formation mechanism could involve the direct decomposition of an AAHP into an anhydride and water.[65] This reaction likely occurs in the gas-phase ozonolysis of ethene in the presence of formic acid.[66] However, this pathway appears to be negligible in the decomposition of AAHPs derived from the ozonolysis of α-pinene SCI with pinonic acid or adipic acid in aqueous phase systems.[65] Another proposed pathway leading to a dehydrated product involves an aldol condensation followed by dehydration.[46] In this mechanism, a CH-acidic carbon would act as a nucleophile and attack an aldehyde, forming a β-hydroxy carbonyl intermediate, which subsequently eliminates water to form an α,β-unsaturated carbonyl compound. However, in the reaction system studied here, such a mechanism is highly unlikely. All potentially nucleophilic carbon centers are part of the cyclopentane ring structure of NDA, and any bond formation would necessarily lead to the generation of a sterically hindered bicyclic structure. Furthermore, the resulting ring system would correspond to a cyclopropane or cyclobutane structure, both of which are energetically disfavored due to pronounced ring strain and significant steric hindrance.

Particle Evaporation Efficiency. Due to the varying surface-to-volume ratios, the investigated particles do not evaporate at the same rate in the vaporizer. The larger the particle volume, the higher the temperature required for complete evaporation within the same residence time in the vaporizer. As shown in Figure 5A, at a very short reaction time of 1.3 s, the intensity maxima of the sum of all particle-derived ions follows this expected trend. As the reaction progresses, the volatility of the particles decreases because the resulting ozonolysis products have significantly lower vapor pressures than the precursor compound NDA. Notably, the maximum evaporation temperature for 30 nm particles shifts significantly toward higher temperatures, making them comparable in volatility to 110 nm particles. To ensure complete gas-phase transfer of all particles, the particle size distribution of the residual particles after the vaporizer was determined at different temperatures using an SMPS, and the fraction of evaporated particle volume was calculated. Figure 5B presents this data alongside the corresponding CI-Orbitrap thermogram. The highest ozone concentration used in this study (10 ppm) and the longest reaction time (106.8 s) in the flow tube at 50% RH were selected for these measurements to ensure representativeness across all experiments. The data show that all examined aerosol particle sizes are completely evaporated at temperatures above 275 °C. Unlike the CI-Orbitrap signal, the particles evaporate in the expected order from 30 to 110 nm particle diameter. However, the differences in the temperature curves are small. The SMPS measurements indicate that the particles already appear to shrink at lower temperatures than expected from the CI-Orbitrap signal. This is likely due to the evaporation of H_2O from the particle phase, which is not detected by the CI-Orbitrap. Overall, the particle evaporation profile closely follows the trend of the thermogram at temperatures above 200 °C, indicating that the transition of the particle-phase molecules into the gas phase is proportional to the increase in signal intensity. We therefore assume that no significant signal loss occurs due to particle evaporation. Therefore, a vaporizer temperature of 285 °C was chosen for the ozonolysis experiments to ensure complete evaporation while maintaining maximum signal intensity.

We were not able to ionize the precursor NDA using nitrate reagent ions, which is likely due to steric hindrance of the polycyclic structure and the oppositely oriented endo and exo carboxyl groups. As a result, the reaction progress with ozone cannot be directly monitored. To ensure a constant aerosol mass in the flow tubes during the experiments, to maintain a consistent ratio with ozone and to enable comparison of absolute signal intensities, TA was used as an internal standard. TA was nebulized together with NDA at a fixed mass ratio; consequently, the TA signal and the signals of the NDA ozonolysis products are subject to the same fluctuations in particle concentration and in the ionization process. Accordingly, the normalization commonly used in CIMS was performed with respect to the TA signal rather than the reagent-ion signal. The relative signals shown are therefore calculated as the quotient of the respective product signal divided by the signal of the internal standard. The mass traces of the ozonolysis products exhibit the same temporal evolution in signal intensity as the TA signal (Figure S8). Thus, the internal standard not only facilitates the correction for signal fluctuations but also enables the differentiation between true signals originating from the reaction system and potential background signals not associated with particle-phase molecules. To verify that TA and the NDA ozonolysis products remained in the particle phase, we also operated the system without the activated-carbon denuder and without the particle evaporator. No gas-phase molecules were detected, indicating that gas-phase partitioning is not significant under the used conditions. It should be noted, however, since TA is a triacid, it can also react with Criegee intermediates formed during ozonolysis reactions, leading to the formation of a TA-AAHP (Figure 3). Although this reaction is observed, it does not lead to a noticeable reduction in the internal standard signal. With a measured maximum contribution of only 1.5% of the total product signal, TA-AAHP is not a significant reaction product. Nevertheless, we have decided to take it into account so that the sum of the internal standard signal and TA-AAHP is used for correction.

Humidity-Dependence of the Reaction Rate. To monitor the progress of the reaction, we examine the total signal, defined as the sum of the detected and normalized ozonolysis product signals. The molecular formulas included in this sum are listed in Table S2. Figure 6 shows the TA-normalized total signal after 106.8 s of reaction, plotted as a function of relative humidity for three ozone concentrations

https://doi.org/10.1021/acsestair.5c00189
ACS EST Air 2025, 2, 2491−2503

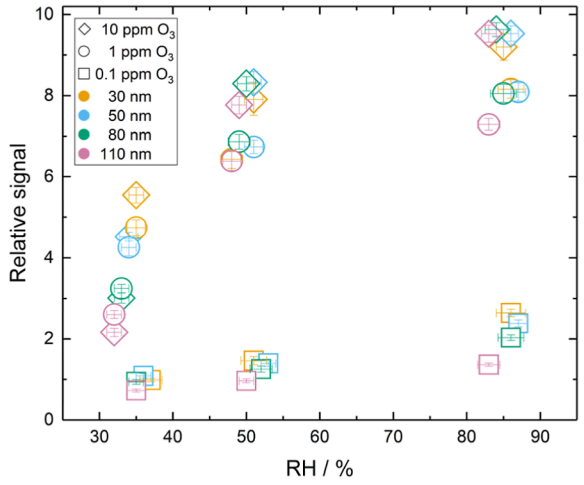

Figure 6. Sum of product signals of the heterogeneous ozonolysis of NDA as a function of RH at a reaction time of 106.8 s, for particles with diameters of 30, 50, 80, and 110 nm and ozone concentrations of 0.1, 1, and 10 ppm. The molecular formulas included in the sum are listed in Table S2.

and four particle sizes. A clear dependence on relative humidity (RH) is observed, with higher humidity leading to higher product signals. Both NDA and TA, as di- and triacids, respectively, are hygroscopic. It therefore suggests that the results can be attributed to the water content and thus the changing phase state of the organic particles. The phase transition from an amorphous solid state under dry conditions to a semisolid state and finally to a liquid state has a major influence on the diffusion coefficients of the reaction partners. At high RH, ozone uptake is driven by reactions throughout the particle volume; at low RH, it is limited to reactions near the particle surface and kinetically limited by slow diffusion and replenishment of unreacted organic molecules.[67] Beyond RH, a dependence on particle size is also evident, particularly under dry conditions at ozone concentrations of 1 and 10 ppm. At the highest ozone concentration, the total signal for 30 nm particles is nearly three times higher than that for 110 nm particles. In general, it can be expected that smaller particles react more rapidly with ozone due to their larger surface-to-volume ratio. However, an additional effect seems to influence the observed kinetics, as illustrated in Figure 7A. This figure illustrates the evolution of the total signal at 35% RH and 10 ppm ozone. After a rapid initial product formation within the first 10 s, the rate of product accumulation slows significantly for the remainder of the reaction period, independent of particle size. One possible explanation for this could be the formation of a crust on the outer particle surface due to lower diffusion rates in dry particles. This crust could hinder the further diffusion of ozone into the particle core and thus effectively limit the reaction to an outer shell region. Such a mechanism would also account for the greater extent of precursor conversion in smaller particles. For instance, if a 4 nm thick crust were to form, approximately 60% of the volume of a 30 nm particle would be affected, whereas only 20% of a 110 nm particle would react. This crusting effect appears to be less pronounced at lower ozone concentrations. At 0.1 ppm of O_3, the relative total signal across all particle sizes is almost identical, and at 1 ppm of O_3, the differences are significantly smaller.

The situation at a relative humidity of 85% is quite different, as can be seen in Figure 7B. Here, particles with a size of 30 nm react the fastest, which was to be expected due to their highest surface-to-volume ratio. However, after a reaction time of 106.8 s, all particle sizes show approximately the same overall signal in the CI Orbitrap. Since the overall signal does not change significantly between the second longest and longest reaction times, with the exception of the 110 nm particles, this suggests that the starting material NDA has already reacted completely with O_3 at this point. This indicates that the higher water content in the particle causes faster diffusion into the interior of the particle and no crust forms.

Particle-Size-Dependent Chemistry. Although all particle sizes show similar total signals at 85% RH, there are still significant deviations in the product distribution of the resulting ozonolysis products. This is illustrated by a few exemplary products in Figure 8. Time profiles of all the signals corresponding to the major NDA ozonolysis−derived molecular formulas are shown in Figures S9−S17. The carbon

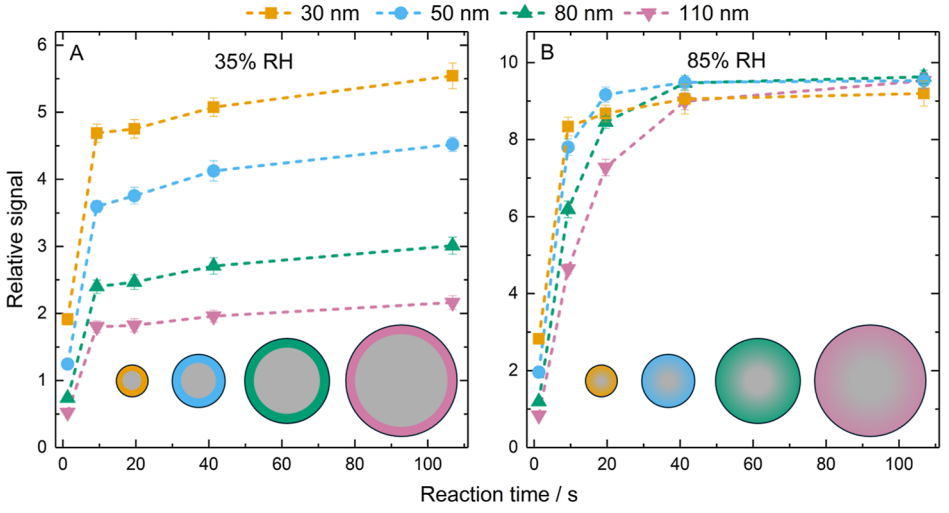

Figure 7. Evolution of the relative total signal of ozonolysis products over the reaction time at 35% RH (A) and 85% RH (B) at 10 ppm of O_3 for particles with diameters of 30, 50, 80, and 110 nm. The molecular formulas included in the total signal are listed in Table S2. The schematic particle illustrations represent the hypothesized formation of a surface crust under dry conditions and unimpeded diffusion under humid conditions.

https://doi.org/10.1021/acsestair.5c00189
ACS EST Air 2025, 2, 2491−2503

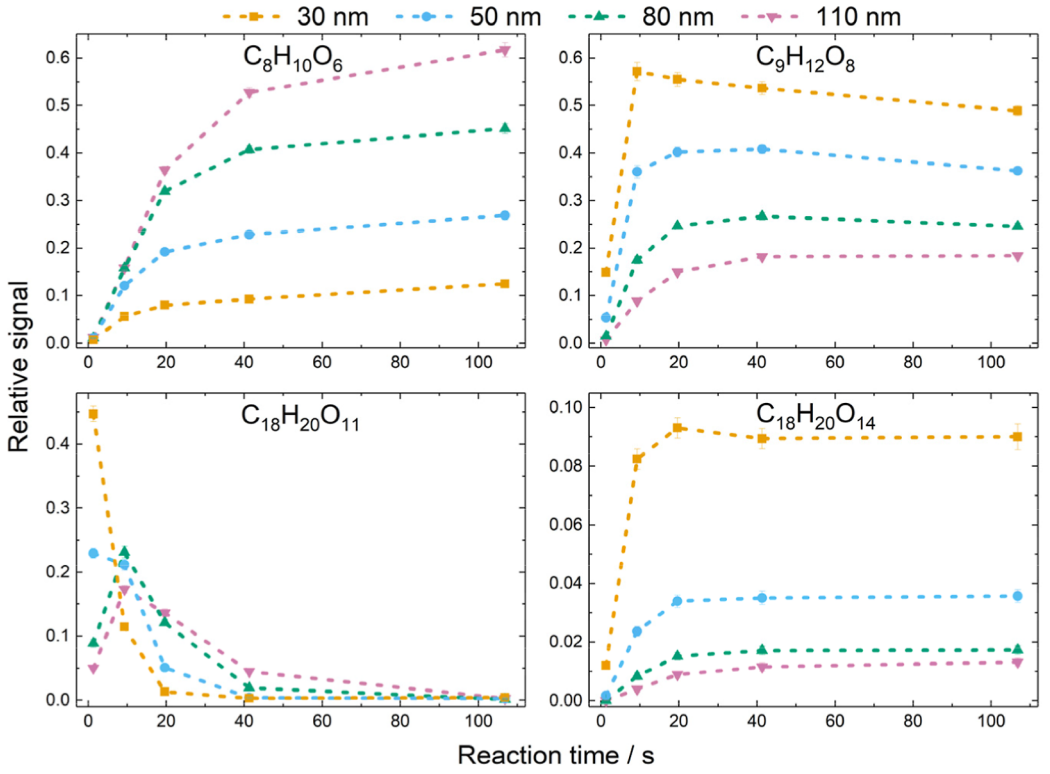

Figure 8. Temporal evolution of selected ozonolysis product signal intensities exhibiting pronounced particle-size-dependent differences (10 ppm of O_3, 85% RH).

loss product with the formula $C_8H_{10}O_6$ (XVIII) forms significantly faster and in larger quantities in larger particles. In contrast, the water addition product $C_9H_{12}O_8$ forms more abundantly in smaller particles. The first-generation dimer $C_{18}H_{20}O_{11}$ (VIII), on the other hand, shows an unusual trend. The signal of this compound increases sharply at short reaction times, but then drops almost as quickly. The time required to reach the maximum signal intensity increases with particle size. In the 30 nm particles, the formation and subsequent decomposition of this dimer are so rapid that the signal already drops even at the shortest reaction time observed. The most likely products formed from this decay are further oxidized aged dimers through reaction with an additional ozone molecule, as well as NDA and $C_9H_{10}O_7$ (II) as decomposition products, or NDA and $C_9H_{12}O_8$ (IV) through hydrolysis.[65] The signal evolution of the aged dimer $C_{18}H_{20}O_{14}$ exhibits the most pronounced particle-size-dependent differences among the compounds shown. The relative signal intensity for 30 nm particles is almost eight times higher than for particles with a diameter of 110 nm. While the particle-size dependency for carbon loss and hydrated products shows an approximately linear trend, the effect for the dimer becomes more pronounced with decreasing particle size. In summary, it can be concluded that smaller particles favor the formation of higher molecular weight products, while decomposition reactions proceed more slowly. This could be due to the higher internal pressure in smaller particles caused by the Laplace pressure.[30] In general, bond-forming reactions, i.e., reactions in which the product side has more bonds than the reactant side, have negative activation volumes. This is due to shorter atomic distances in covalent-bonded molecules compared to van der Waals interactions, a property that is also exploited in high-pressure synthesis.[28] If smaller particles have higher internal pressure due to Laplace pressure, this would explain the significantly higher proportion of compounds with higher molecular weight. Another explanation could be the influence of the pH in the particles, although the data here is somewhat contradictory. Studies have shown that smaller aerosol particles are more acidic and have a higher pH gradient between the surface and the bulk.[68,69] Other studies suggest that the degradation of HAHPs is favored by lower pH values, while the degradation of bimolecular AAHPs occurs more rapidly at higher pH values.[52,65] The latter could explain the lower proportion of bimolecular AAHPs in the larger particles, as these should be less acidic than the smaller particles. However, this is not consistent with the results found here, which show that more hydrated product is present in the smaller particles. This would have to be the opposite if the decomposition of HAHPs occurs faster under acidic conditions. In conclusion, our results provide direct evidence for particle-size-dependent chemistry in the studied heterogeneous reactions. The mechanistic origins of these size dependencies, however, are not yet fully resolved, and further studies specifically designed to address these questions are warranted.

Influence of Relative Humidity on the Product Distribution. The particle-size-dependent differences observed at 85% RH are also found at the other investigated humidities (Figure 9). This figure presents the distribution of the various product groups for 30 and 110 nm particles after 106.8 s of reaction time across three RH conditions at 10 ppm ozone. As previously noted in Figure 8, the most pronounced differences in product signals between particle sizes occur between those with the largest diameter disparity. This trend is consistent across all examined RH levels and ozone concentrations. Consequently, only the data for 30 and 110

https://doi.org/10.1021/acsestair.5c00189
ACS EST Air 2025, 2, 2491−2503

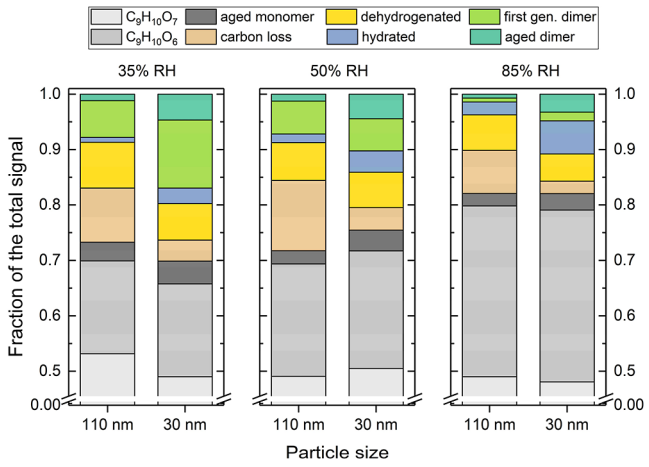

Figure 9. Product distribution of the total signal from the heterogeneous ozonolysis of NDA after 106.8 s at 10 ppm of O_3 for particles with diameters of 30 and 110 nm and relative humidities of 35%, 50% and 85%. The molecular formulas included in the total signal, and their assignments to the different product classes, are listed in Table S2.

nm particles is displayed, with signals for 50 and 80 nm particles falling intermediate to these values.

The proportion of hydrated products, with the main product being $C_9H_{12}O_8$, is consistently higher in the 30 nm particles. Across all particle sizes, the proportion decreases with drier reaction conditions, which is expected since we assume these are reaction products involving H_2O. Therefore, the size-dependent differences could also stem from varying water content within the particles depending on the particle diameter. However, this is contradicted by the measured signal of the first-generation product $C_9H_{10}O_6$ (V). Previous studies have demonstrated that the proportion of this ozonolysis product increases with higher humidity levels,[46,70] which is anticipated since its formation in the particle phase likely involves water. This influence is also evident in our results, as the proportion is much higher at 85% RH than under drier conditions. However, there is no clear size dependence for $C_9H_{10}O_6$. Therefore, a varying water content in the particles is unlikely to explain the observed differences.

The dehydrogenated products show the opposite dependence on RH as the hydrated products. As depicted in Figure 4, these products likely form either through the elimination of H_2 or H_2O from the AAHP $C_9H_{10}O_7$ (II) via the formation of a cyclic peroxyhemiacetal (XIX). Therefore, if water is eliminated during the reaction, it is reasonable to expect higher product formation under dry conditions. Moreover, the decomposition pathway likely involves the formation of anhydrides, which are expected to rapidly hydrolyze back to their corresponding acids under humid conditions. Interestingly, the proportion of these decomposition products, similar to the carbon loss products, is higher in larger particles. As with the hydrated products, the formation of the cyclic intermediate appears to play a crucial role. The effect of particle size is less pronounced here compared to other products, possibly because the decomposition reaction likely proceeds through the formation of the cyclic peroxyhemiacetal, which we suspect is preferentially formed in smaller particles (Laplace pressure). Thus, two opposing particle-size-dependent effects may be at play: the formation of the cyclic peroxyhemiacetal, favored in smaller particles, and its decomposition, favored in larger particles.

The particle-size dependency of the carbon loss product $C_8H_{10}O_6$ (XVIII) at 85% RH was previously shown in Figure 8. This dependency of higher amounts in larger particles is also observed for the entire carbon loss product group across all investigated RH levels. However, these products exhibit a particular dependency on RH, being most abundant under moderate conditions of 50% RH. We hypothesize that these products are alcohols resulting from the hydrolysis of esters formed during the Baeyer–Villiger oxidation. Typically, ester hydrolysis should be more favorable under humid conditions, whereas Baeyer–Villiger oxidation is anticipated to be more intensive under dry conditions.[56] Therefore, the moderate humidity range could be the ideal condition where enough esters are formed, but there is also sufficient water in the particle phase to enable rapid hydrolysis. This hypothesis is further supported by the observation that the aged monomer group in Figure 9 also exhibits the highest proportions at 35% and 50% RH. The proposed products of the Baeyer–Villiger oxidation, the tetraacid (XV) and the formic acid ester (XVI), both with the molecular formula $C_9H_{10}O_8$, constitute the largest fraction of this aged monomer group. Furthermore, this group exhibits the inverse particle-size dependence, with higher fractions of aged monomers observed in smaller particles. Preferential hydrolysis of the esters within this group in the 110 nm particles could explain the observed differences.

A clear particle-size dependence is also evident for the bimolecular reaction products (green product groups in Figure 9) across all investigated RHs. This effect is most pronounced for the highly oxidized aged dimer group, whose contribution in 30 nm particles is consistently at least three times greater than in 110 nm particles. One possible cause for the high fraction of bimolecular reaction products could again be the effect of increased internal pressure within smaller particles, favoring dimer formation. An increased formation of first-generation dimers would consequently lead to higher levels of aged dimers.

CONCLUSION

The heterogeneous ozonolysis of NDA leads to a complex series of reaction products that depend heavily on relative humidity, particle size, and reaction time. The tentatively assigned first-generation products include a dialdehyde, a tricarboxylic acid, and a monomolecular and a bimolecular α-hydroxyalkyl hydroperoxide, which appear to undergo further oxidation, decomposition, and hydrolysis reactions. Particle-phase aging mechanisms such as Baeyer–Villiger oxidation, hydroperoxide-driven oxidation, and decomposition of AAHPs could play a crucial role in the formation of the final product distribution. Our results show that relative humidity strongly influences the proposed reaction pathways. Higher relative humidity promotes hydrolysis reactions, leading to an increased formation of hydrated species and a lower dimer fraction. Lower relative humidity, on the other hand, favors the formation of anhydrides and slows down decomposition reactions. The observed strong particle-size dependence of several product groups motivates the hypothesis that Laplace pressure could play a role in influencing chemical reactivity. In smaller particles, dimerization is enhanced, leading to a higher proportion of oligomeric species. This trend could be caused by the increased internal pressure in these particles, which is known to favor bond-forming reactions, as these often have

https://doi.org/10.1021/acsestair.5c00189
ACS EST Air 2025, 2, 2491–2503

negative activation volumes. Conversely, larger particles exhibit higher proportions of decomposition products, especially those formed by hydrolysis and leading to carbon loss products, as well as dehydrated products due to the loss of H_2 or H_2O.

Overall, our results highlight the importance of particle size and humidity for the chemical processing of organic aerosol particles. The interaction of these factors influences not only the volatility and chemical composition of the particles, but also their potential to form highly oxidized and low-volatile products, an observation that may be particularly relevant for understanding the early growth phase of aerosol particles in the nanometer range—and thus their survival probability. The results underscore the need for further studies that explicitly consider particle-size effects and multiphase processes in order to better understand the role of organic substances in atmospheric new particle formation.

■ ASSOCIATED CONTENT

Supporting Information

The Supporting Information is available free of charge at https://pubs.acs.org/doi/10.1021/acsestair.5c00189.

Additional details on the thermal decomposition in the particle evaporator, particle number distributions, the design and effectiveness of the gas cooling unit and the classification of NDA ozonolysis products, their temporal evolution and MS/MS spectra (PDF)

■ AUTHOR INFORMATION

Corresponding Author

Thorsten Hoffmann − *Department of Chemistry, Johannes Gutenberg University, 55128 Mainz, Germany;* orcid.org/0000-0003-0939-271X; Email: hoffmant@uni-mainz.de

Author

Marcel Douverne − *Department of Chemistry, Johannes Gutenberg University, 55128 Mainz, Germany*

Complete contact information is available at: https://pubs.acs.org/10.1021/acsestair.5c00189

Notes

The authors declare no competing financial interest.

■ ACKNOWLEDGMENTS

The study was supported through the German Research Foundation (DFG) Reinhart Koselleck-Project HO 1748/19-1 and the Max Planck Graduate Center Mainz.

■ REFERENCES

(1) Andreae, M. O. The Aerosol Nucleation Puzzle. *Science* **2013**, *339* (6122), 911−912.

(2) Bianchi, F.; Trostl, J.; Junninen, H.; Frege, C.; Henne, S.; Hoyle, C. R.; Molteni, U.; Herrmann, E.; Adamov, A.; Bukowiecki, N.; Chen, X.; Duplissy, J.; Gysel, M.; Hutterli, M.; Kangasluoma, J.; Kontkanen, J.; Kuerten, A.; Manninen, H. E.; Muench, S.; Perakyla, O.; Petaja, T.; Rondo, L.; Williamson, C.; Weingartner, E.; Curtius, J.; Worsnop, D. R.; Kulmala, M.; Dommen, J.; Baltensperger, U. New particle formation in the free troposphere:A question of chemistry and timing. *Science* **2016**, *352* (6289), 1109−1112.

(3) Williamson, C. J.; Kupc, A.; Axisa, D.; Bilsback, K. R.; Bui, T.; Campuzano-Jost, P.; Dollner, M.; Froyd, K. D.; Hodshire, A. L.; Jimenez, J. L.; Kodros, J. K.; Luo, G.; Murphy, D. M.; Nault, B. A.; Ray, E. A.; Weinzierl, B.; Wilson, J. C.; Yu, F.; Yu, P.; Pierce, J. R.; Brock, C. A. A large source of cloud condensation nuclei from new particle formation in the tropics. *Nature* **2019**, *574* (7778), 399.

(4) Curtius, J.; Heinritzi, M.; Beck, L. J.; Pöhlker, M. L.; Tripathi, N.; Krumm, B. E.; Holzbeck, P.; Nussbaumer, C. M.; Hernández Pardo, L.; Klimach, T.; Barmpounis, K.; Andersen, S. T.; Bardakov, R.; Bohn, B.; Cecchini, M. A.; Chaboureau, J.-P.; Dauhut, T.; Dienhart, D.; Dörich, R.; Edtbauer, A.; Giez, A.; Hartmann, A.; Holanda, B. A.; Joppe, P.; Kaiser, K.; Keber, T.; Klebach, H.; Krüger, O. O.; Kürten, A.; Mallaun, C.; Marno, D.; Martinez, M.; Monteiro, C.; Nelson, C.; Ort, L.; Raj, S. S.; Richter, S.; Ringsdorf, A.; Rocha, F.; Simon, M.; Sreekumar, S.; Tsokankunku, A.; Unfer, G. R.; Valenti, I. D.; Wang, N.; Zahn, A.; Zauner-Wieczorek, M.; Albrecht, R. I.; Andreae, M. O.; Artaxo, P.; Crowley, J. N.; Fischer, H.; Harder, H.; Herdies, D. L.; Machado, L. A. T.; Pöhlker, C.; Pöschl, U.; Possner, A.; Pozzer, A.; Schneider, J.; Williams, J.; Lelieveld, J. Isoprene nitrates drive new particle formation in Amazon's upper troposphere. *Nature* **2024**, *636* (8041), 124−130.

(5) Chen, L.; Yousaf, M.; Xu, J.; Ma, X.; Zhou, X.; Li, G.; Symonds, J.; Chen, R.; Tang, S.; Salehi, F.; Njue, J. C. W.; Lelieveld, J. Ultrafine particles deposition in human respiratory tract:Experimental measurement and modeling. *Ecotoxicol. Environ. Saf.* **2025**, *295*, 118123.

(6) Ehn, M.; Thornton, J. A.; Kleist, E.; Sipilä, M.; Junninen, H.; Pullinen, I.; Springer, M.; Rubach, F.; Tillmann, R.; Lee, B.; Lopez-Hilfiker, F.; Andres, S.; Acir, I.-H.; Rissanen, M.; Jokinen, T.; Schobesberger, S.; Kangasluoma, J.; Kontkanen, J.; Nieminen, T.; Kurtén, T.; Nielsen, L. B.; Jørgensen, S.; Kjaergaard, H. G.; Canagaratna, M.; Maso, M. D.; Berndt, T.; Petäjä, T.; Wahner, A.; Kerminen, V.-M.; Kulmala, M.; Worsnop, D. R.; Wildt, J.; Mentel, T. F. A large source of low-volatility secondary organic aerosol. *Nature* **2014**, *506* (7489), 476−479.

(7) Kirkby, J.; Duplissy, J.; Sengupta, K.; Frege, C.; Gordon, H.; Williamson, C.; Heinritzi, M.; Simon, M.; Yan, C.; Almeida, J.; Troestl, J.; Nieminen, T.; Ortega, I. K.; Wagner, R.; Adamov, A.; Amorim, A.; Bernhammer, A.-K.; Bianchi, F.; Breitenlechner, M.; Brilke, S.; Chen, X.; Craven, J.; Dias, A.; Ehrhart, S.; Flagan, R. C.; Franchin, A.; Fuchs, C.; Guida, R.; Hakala, J.; Hoyle, C. R.; Jokinen, T.; Junninen, H.; Kangasluoma, J.; Kim, J.; Krapf, M.; Kuerten, A.; Laaksonen, A.; Lehtipalo, K.; Makhmutov, V.; Mathot, S.; Molteni, U.; Onnela, A.; Peraekylae, O.; Piel, F.; Petaejae, T.; Praplan, A. P.; Pringle, K.; Rap, A.; Richards, N. A. D.; Riipinen, I.; Rissanen, M. P.; Rondo, L.; Sarnela, N.; Schobesberger, S.; Scott, C. E.; Seinfeld, J. H.; Sipilae, M.; Steiner, G.; Stozhkov, Y.; Stratmann, F.; Tome, A.; Virtanen, A.; Vogel, A. L.; Wagner, A. C.; Wagner, P. E.; Weingartner, E.; Wimmer, D.; Winkler, P. M.; Ye, P.; Zhang, X.; Hansel, A.; Dommen, J.; Donahue, N. M.; Worsnop, D. R.; Baltensperger, U.; Kulmala, M.; Carslaw, K. S.; Curtius, J. Ion-induced nucleation of pure biogenic particles. *Nature* **2016**, *533* (7604), 521.

(8) Hong, J.; Ma, J.; Ma, N.; Shi, J.; Xu, W.; Zhang, G.; Zhu, S.; Zhang, S.; Tang, M.; Pan, X.; Xie, L.; Li, G.; Kuhn, U.; Yan, C.; Qi, X.; Zha, Q.; Nie, W.; Tao, J.; He, Y.; Zhou, Y.; Sun, Y.; Xu, H.; Liu, L.; Cai, R.; Zhou, G.; Kuang, Y.; Yuan, B.; Wang, Q.; Petäjä, T.; Kerminen, V.-M.; Kulmala, M.; Cheng, Y.; Su, H. Low Hygroscopicity of Newly Formed Particles on the North China Plain and Its Implications for Nanoparticle Growth. *Geophys. Res. Lett.* **2024**, *51* (14), No. e2023GL107516.

(9) Stolzenburg, D.; Sarnela, N.; Bianchi, F.; Cai, J.; Cai, R.; Cheng, Y.; Dada, L.; Donahue, N. M.; Grothe, H.; Holm, S.; Kerminen, V.-M.; Lehtipalo, K.; Petäjä, T.; Sulo, J.; Winkler, P. M.; Yan, C.; Kangasluoma, J.; Kulmala, M. Incomplete mass closure in atmospheric nanoparticle growth. *npj Clim. Atmos. Sci.* **2025**, *8* (1), 75.

(10) Li, X.; Li, Y.; Cai, R.; Yan, C.; Qiao, X.; Guo, Y.; Deng, C.; Yin, R.; Chen, Y.; Li, Y.; Yao, L.; Sarnela, N.; Zhang, Y.; Petäjä, T.; Bianchi, F.; Liu, Y.; Kulmala, M.; Hao, J.; Smith, J. N.; Jiang, J. Insufficient Condensable Organic Vapors Lead to Slow Growth of New Particles in an Urban Environment. *Environ. Sci. Technol.* **2022**, *56* (14), 9936−9946.

(11) Dam, M.; Thomas, A. E.; Smith, J. N. Formation of Highly Oxidized Organic Compounds and Secondary Organic Aerosol from α-Thujene Ozonolysis. *J. Phys. Chem. A* **2023**, *127* (33), 6989−6998.
(12) Berndt, T.; Hoffmann, E. H.; Tilgner, A.; Herrmann, H. Highly oxidized products from the atmospheric reaction of hydroxyl radicals with isoprene. *Nat. Commun.* **2025**, *16* (1), 2068.
(13) Zhao, J.; Häkkinen, E.; Graeffe, F.; Krechmer, J. E.; Canagaratna, M. R.; Worsnop, D. R.; Kangasluoma, J.; Ehn, M. A combined gas- and particle-phase analysis of highly oxygenated organic molecules (HOMs) from α -pinene ozonolysis. *Atmos. Chem. Phys.* **2023**, *23* (6), 3707−3730.
(14) Shen, H.; Vereecken, L.; Kang, S.; Pullinen, I.; Fuchs, H.; Zhao, D.; Mentel, T. F. Unexpected significance of a minor reaction pathway in daytime formation of biogenic highly oxygenated organic compounds. *Sci. Adv.* **2022**, *8* (42), No. eabp8702.
(15) Bianchi, F.; Kurtén, T.; Riva, M.; Mohr, C.; Rissanen, M. P.; Roldin, P.; Berndt, T.; Crounse, J. D.; Wennberg, P. O.; Mentel, T. F.; Wildt, J.; Junninen, H.; Jokinen, T.; Kulmala, M.; Worsnop, D. R.; Thornton, J. A.; Donahue, N.; Kjaergaard, H. G.; Ehn, M. Highly Oxygenated Organic Molecules (HOM) from Gas-Phase Autoxidation Involving Peroxy Radicals: A Key Contributor to Atmospheric Aerosol. *Chem. Rev.* **2019**, *119* (6), 3472−3509.
(16) Stolzenburg, D.; Fischer, L.; Vogel, A. L.; Heinritzi, M.; Schervish, M.; Simon, M.; Wagner, A. C.; Dada, L.; Ahonen, L. R.; Amorim, A.; Baccarini, A.; Bauer, P. S.; Baumgartner, B.; Bergen, A.; Bianchi, F.; Breitenlechner, M.; Brilke, S.; Buenrostro Mazon, S.; Chen, D.; Dias, A.; Draper, D. C.; Duplissy, J.; El Haddad, I.; Finkenzeller, H.; Frege, C.; Fuchs, C.; Garmash, O.; Gordon, H.; He, X.; Helm, J.; Hofbauer, V.; Hoyle, C. R.; Kim, C.; Kirkby, J.; Kontkanen, J.; Kürten, A.; Lampilahti, J.; Lawler, M.; Lehtipalo, K.; Leiminger, M.; Mai, H.; Mathot, S.; Mentler, B.; Molteni, U.; Nie, W.; Nieminen, T.; Nowak, J. B.; Ojdanic, A.; Onnela, A.; Passananti, M.; Petäjä, T.; Quéléver, L. L. J.; Rissanen, M. P.; Sarnela, N.; Schallhart, S.; Tauber, C.; Tomé, A.; Wagner, R.; Wang, M.; Weitz, L.; Wimmer, D.; Xiao, M.; Yan, C.; Ye, P.; Zha, Q.; Baltensperger, U.; Curtius, J.; Dommen, J.; Flagan, R. C.; Kulmala, M.; Smith, J. N.; Worsnop, D. R.; Hansel, A.; Donahue, N. M.; Winkler, P. M. Rapid growth of organic aerosol nanoparticles over a wide tropospheric temperature range. *Proc. Natl. Acad. Sci. U.S.A.* **2018**, *115* (37), 9122−9127.
(17) Kenseth, C. M.; Hafeman, N. J.; Rezgui, S. P.; Chen, J.; Huang, Y.; Dalleska, N. F.; Kjaergaard, H. G.; Stoltz, B. M.; Seinfeld, J. H.; Wennberg, P. O. Particle-phase accretion forms dimer esters in pinene secondary organic aerosol. *Science (New York, N.Y.)* **2023**, *382* (6672), 787−792.
(18) Kenseth, C. M.; Hafeman, N. J.; Huang, Y.; Dalleska, N. F.; Stoltz, B. M.; Seinfeld, J. H. Synthesis of Carboxylic Acid and Dimer Ester Surrogates to Constrain the Abundance and Distribution of Molecular Products in α-Pinene and β-Pinene Secondary Organic Aerosol. *Environ. Sci. Technol.* **2020**, *54* (20), 12829−12839.
(19) Kenseth, C. M.; Huang, Y.; Zhao, R.; Dalleska, N. F.; Hethcox, C.; Stoltz, B. M.; Seinfeld, J. H. Synergistic O3 + OH oxidation pathway to extremely low-volatility dimers revealed in β-pinene secondary organic aerosol. *Proc. Natl. Acad. Sci. U.S.A.* **2018**, *115* (33), 8301−8306.
(20) Pierce, J. R.; Riipinen, I.; Kulmala, M.; Ehn, M.; Petäjä, T.; Junninen, H.; Worsnop, D. R.; Donahue, N. M. Quantification of the volatility of secondary organic compounds in ultrafine particles during nucleation events. *Atmos. Chem. Phys.* **2011**, *11* (17), 9019−9036.
(21) de la Puente, M.; Laage, D. How the Acidity of Water Droplets and Films Is Controlled by the Air-Water Interface. *J. Am. Chem. Soc.* **2023**, *145* (46), 25186−25194.
(22) Martins-Costa, M. T. C.; Ruiz-Lopez, M. F. Electrostatics and Chemical Reactivity at the Air-Water Interface. *J. Am. Chem. Soc.* **2023**, *145*, 1400.
(23) Lacour, R. A.; Heindel, J. P.; Zhao, R.; Head-Gordon, T. The Role of Interfaces and Charge for Chemical Reactivity in Microdroplets. *J. Am. Chem. Soc.* **2025**, *147* (8), 6299−6317.
(24) Mehrgardi, M. A.; Mofidfar, M.; Zare, R. N. Sprayed Water Microdroplets Are Able to Generate HydrogenPeroxide Spontaneously. *J. Am. Chem. Soc.* **2022**, *144* (17), 7606−7609.
(25) Eatoo, M. A.; Mishra, H. Busting the myth of spontaneous formation of H2O2 at the air-water interface:Contributions of the liquid-solid interface and dissolved oxygen exposed. *Chem. Sci.* **2024**, *15* (9), 3093.
(26) Angelaki, M.; d'Erceville, J.; Donaldson, D. J.; George, C. pH. Affects the Spontaneous Formation of H2O2 at the Air-Water Interfaces. *J. Am. Chem. Soc.* **2024**, *146* (38), 25889−25893.
(27) Cheng, Y.; Su, H.; Koop, T.; Mikhailov, E.; Pöschl, U. Size dependence of phase transitions in aerosol nanoparticles. *Nat. Commun.* **2015**, *6*, 5923.
(28) van Eldik, R. *High Pressure Chemistry:Synthetic, Mechanistic, and Supercritical Applications*, 1st ed.; John Wiley & Sons Incorporated, 2008.
(29) Riva, M.; Sun, J.; McNeill, V. F.; Ragon, C.; Perrier, S.; Rudich, Y.; Nizkorodov, S. A.; Chen, J.; Caupin, F.; Hoffmann, T.; George, C. High Pressure Inside Nanometer-Sized Particles Influences the Rate and Products of Chemical Reactions. *Environ. Sci. Technol.* **2021**, *55*, 7786.
(30) Petters, S. S. Constraints on the Role of Laplace Pressure in Multiphase Reactions and Viscosity of Organic Aerosols. *Geophys. Res. Lett.* **2022**, *49* (12), No. e2022GL098959.
(31) Dubois, C.; Perrier, S.; George, C.; Riva, M. The High Pressure Inside Aerosol Particles Enhances Photochemical Reactions of Biomass Burning Compounds. *ACS Earth Space Chem.* **2024**, *8* (5), 1062−1071.
(32) Li, X.; Cai, R.; Hao, J.; Smith, J. N.; Jiang, J. Online detection of airborne nanoparticle composition with mass spectrometry:Recent advances, challenges, and opportunities. *TrAC, Trends Anal. Chem.* **2023**, *166*, 117195.
(33) Thomas, A. E.; Glicker, H. S.; Guenther, A. B.; Seco, R.; Vega Bustillos, O.; Tota, J.; Souza, R. A. F.; Smith, J. N. Seasonal investigation of ultrafine-particle organic composition in an eastern Amazonian rainforest. *Atmos. Chem. Phys.* **2025**, *25* (2), 959−977.
(34) Kugel, R. W.; Ault, B. S. Infrared matrix isolation and theoretical studies of reactions of ozone with bicyclic alkenes: α-pinene, norbornene, and norbornadiene. *J. Phys. Chem. A* **2015**, *119* (2), 312−322.
(35) Witkowski, B.; Jurdana, S.; Gierczak, T. Limononic Acid Oxidation by Hydroxyl Radicals and Ozone in the Aqueous Phase. *Environ. Sci. Technol.* **2018**, *52* (6), 3402−3411.
(36) Witkowski, B.; Al-Sharafi, M.; Gierczak, T. Ozonolysis of β-Caryophyllonic and Limononic Acids in the Aqueous Phase: Kinetics, Product Yield, and Mechanism. *Environ. Sci. Technol.* **2019**, *53* (15), 8823−8832.
(37) Mamakos, A. Methodology to quantify the ratio of multiple-to single-charged fractions acquired in aerosol neutralizers. *Aerosol Sci. Technol.* **2016**, *50* (4), 363−372.
(38) Guo, Q.; Hu, W.; Hu, M.; Wang, Y.; Guo, S.; Wu, Z.; Zheng, J.; Zeng, L. Bulk Quantification and Molecular Characterization of Thermal Decomposition from the Thermal Desorption of Organic Aerosol. *ACS ES&T Air* **2024**, *1* (7), 628−636.
(39) Yang, L. H.; Takeuchi, M.; Chen, Y.; Ng, N. L. Characterization of thermal decomposition of oxygenated organic compounds in FIGAERO-CIMS. *Aerosol Sci. Technol.* **2021**, *55* (12), 1321−1342.
(40) Riva, M.; Ehn, M.; Li, D.; Tomaz, S.; Bourgain, F.; Perrier, S.; George, C. CI-Orbitrap: An Analytical Instrument To Study Atmospheric Reactive Organic Species. *Anal. Chem.* **2019**, *91* (15), 9419−9423.
(41) Riva, M.; Bruggemann, M.; Li, D.; Perrier, S.; George, C.; Herrmann, H.; Berndt, T. Capability of CI-Orbitrap for Gas-Phase Analysis in Atmospheric Chemistry:A Comparison with the Cl-APi-TOF Technique. *Anal. Chem.* **2020**, *92* (12), 8142−8150.
(42) Zhao, J.; Mickwitz, V.; Luo, Y.; Häkkinen, E.; Graeffe, F.; Zhang, J.; Timonen, H.; Canagaratna, M.; Krechmer, J. E.; Zhang, Q.; Kulmala, M.; Kangasluoma, J.; Worsnop, D.; Ehn, M. Characterization of the Vaporization Inlet for Aerosols (VIA) for online

https://doi.org/10.1021/acsestair.5c00189
ACS EST Air 2025, 2, 2491−2503

measurements of particulate highly oxygenated organic molecules (HOMs). *Atmos. Meas. Tech.* **2024**, *17* (5), 1527−1543.
(43) Cai, R.; Li, Y.; Clément, Y.; Li, D.; Dubois, C.; Fabre, M.; Besson, L.; Perrier, S.; George, C.; Ehn, M.; Huang, C.; Yi, P.; Ma, Y.; Riva, M. Orbitool: a software tool for analyzing online Orbitrap mass spectrometry data. *Atmos. Meas. Tech.* **2021**, *14* (3), 2377−2387.
(44) Criegee, R. Mechanism of Ozonolysis. *Angew Chem. Int. Ed. Engl.* **1975**, *14* (11), 745−752.
(45) Testero, S. A.; Mangione, M. I.; Poeylaut-Palena, A. A.; Sierra, M. G.; Spanevello, R. A. Unsymmetrical ozonolysis of carbohydrate derived norbornene systems. *Tetrahedron* **2007**, *63* (46), 11410−11420.
(46) Zhao, Z.; Xu, Q.; Yang, X.; Zhang, H. Heterogeneous Ozonolysis of Endocyclic Unsaturated Organic Aerosol Proxies: Implications for Criegee Intermediate Dynamics and Later-Generation Reactions. *ACS Earth Space Chem.* **2019**, *3* (3), 344−356.
(47) Wang, S.; Zhao, Y.; Chan, A. W. H.; Yao, M.; Chen, Z.; Abbatt, J. P. D. Organic Peroxides in Aerosol: Key Reactive Intermediates for Multiphase Processes in the Atmosphere. *Chem. Rev.* **2023**, *123*, 1635.
(48) Enami, S. Fates of Organic Hydroperoxides in Atmospheric Condensed Phases. *J. Phys. Chem. A* **2021**, *125* (21), 4513−4523.
(49) Leviss, D. H.; van Ry, D. A.; Hinrichs, R. Z. Multiphase Ozonolysis of Aqueous α-Terpineol. *Environ. Sci. Technol.* **2016**, *50* (21), 11698−11705.
(50) Riva, M.; Healy, R. M.; Tomaz, S.; Flaud, P.-M.; Perraudin, E.; Wenger, J. C.; Villenave, E. Gas and particulate phase products from the ozonolysis of acenaphthylene. *Atmos. Environ.* **2016**, *142*, 104−113.
(51) Qiu, J.; Fujita, M.; Tonokura, K.; Enami, S. Stability of Terpenoid-Derived Secondary Ozonides in Aqueous Organic Media. *J. Phys. Chem. A* **2022**, *126* (32), 5386−5397.
(52) Qiu, J.; Tonokura, K.; Enami, S. Proton-Catalyzed Decomposition of α-Hydroxyalkyl-Hydroperoxides in Water. *Environ. Sci. Technol.* **2020**, *54* (17), 10561−10569.
(53) Rissanen, M. P.; Kurtén, T.; Sipilä, M.; Thornton, J. A.; Kangasluoma, J.; Sarnela, N.; Junninen, H.; Jørgensen, S.; Schallhart, S.; Kajos, M. K.; Taipale, R.; Springer, M.; Mentel, T. F.; Ruuskanen, T.; Petäjä, T.; Worsnop, D. R.; Kjaergaard, H. G.; Ehn, M. The formation of highly oxidized multifunctional products in the ozonolysis of cyclohexene. *J. Am. Chem. Soc.* **2014**, *136* (44), 15596−15606.
(54) Greenspan, F. P. The Convenient Preparation of Per-acids. *J. Am. Chem. Soc.* **1946**, *68* (5), 907.
(55) Pagonis, D.; Ziemann, P. J. Chemistry of hydroperoxycarbonyls in secondary organic aerosol. *Aerosol Sci. Technol.* **2018**, *52* (10), 1178−1193.
(56) Pospisilova, V.; Lopez-Hilfiker, F. D.; Bell, D. M.; El Haddad, I.; Mohr, C.; Huang, W.; Heikkinen, L.; Xiao, M.; Dommen, J.; Prevot, A. S. H.; Baltensperger, U.; Slowik, J. G. On the fate of oxygenated organic molecules in atmospheric aerosol particles. *Sci. Adv.* **2020**, *6* (11), No. eaax8922.
(57) Lehtinen, C.; Nevalainen, V.; Brunow, G. Experimental and Computational Studies on Substituent Effects in Reactions of Peracid−Aldehyde Adducts. *Tetrahedron* **2000**, *56* (47), 9375−9382.
(58) Lehtinen, C.; Nevalainen, V.; Brunow, G. Experimental and computational studies on solvent effects in reactions of peracid−aldehyde adducts. *Tetrahedron* **2001**, *57* (22), 4741−4751.
(59) Snowden, M.; Bermudez, A.; Kelly, D. R.; Radkiewicz-Poutsma, J. L. The preference for anti over Gauche migration in the Baeyer-Villiger reaction. *J. Org. Chem.* **2004**, *69* (21), 7148−7156.
(60) Barrero, A. F.; Alvarez-Manzaneda, E. J.; Alvarez-Manzaneda, R.; Chahboun, R.; Meneses, R.; Aparicio B, M. Ring A Functionalization of Terpenoids by the Unusual Baeyer-Villiger Rearrangement of Aliphatic Aldehydes. *Synlett* **1999**, *1999* (6), 713−716.
(61) Marteau, C.; Ruyffelaere, F.; Aubry, J.-M.; Penverne, C.; Favier, D.; Nardello-Rataj, V. Oxidative degradation of fragrant aldehydes. Autoxidation by molecular oxygen. *Tetrahedron* **2013**, *69* (10), 2268−2275.
(62) Durham, L. J.; Wurster, C. F.; Mosher, H. S. Peroxides. VIII. The Mechanism for the Thermal Decomposition of n-Butyl Hydroperoxide and n-Butyl 1-Hydroxybutyl Peroxide[1]. *J. Am. Chem. Soc.* **1958**, *80* (2), 332−337.
(63) Claflin, M. S.; Krechmer, J. E.; Hu, W.; Jimenez, J. L.; Ziemann, P. J. Functional Group Composition of Secondary Organic Aerosol Formed from Ozonolysis of α-Pinene Under High VOC and Autoxidation Conditions. *ACS Earth Space Chem.* **2018**, *2* (11), 1196−1210.
(64) Bakker-Arkema, J. G.; Ziemann, P. J. Measurements of Kinetics and Equilibria for the Condensed Phase Reactions of Hydroperoxides with Carbonyls to Form Peroxyhemiacetals. *ACS Earth Space Chem.* **2020**, *4* (3), 467−475.
(65) Zhao, R.; Kenseth, C. M.; Huang, Y.; Dalleska, N. F.; Kuang, X. M.; Chen, J.; Paulson, S. E.; Seinfeld, J. H. Rapid Aqueous-Phase Hydrolysis of Ester Hydroperoxides Arising from Criegee Intermediates and Organic Acids. *J. Phys. Chem. A* **2018**, *122* (23), 5190−5201.
(66) Neeb, P.; Horie, O.; Moortgat, G. K. Gas-phase ozonolysis of ethene in the presence of hydroxylic compounds. *Int. J. Chem. Kinet.* **1996**, *28* (10), 721−730.
(67) Berkemeier, T.; Steimer, S. S.; Krieger, U. K.; Peter, T.; Pöschl, U.; Ammann, M.; Shiraiwa, M. Ozone uptake on glassy, semi-solid and liquid organic matter and the role of reactive oxygen intermediates in atmospheric aerosol chemistry. *Phys. Chem. Chem. Phys.* **2016**, *18* (18), 12662−12674.
(68) Craig, R. L.; Peterson, P. K.; Nandy, L.; Lei, Z.; Hossain, M. A.; Camarena, S.; Dodson, R. A.; Cook, R. D.; Dutcher, C. S.; Ault, A. P. Direct Determination of Aerosol pH: Size-Resolved Measurements of Submicrometer and Supermicrometer Aqueous Particles. *Anal. Chem.* **2018**, *90* (19), 11232−11239.
(69) Gong, K.; Ao, J.; Li, K.; Liu, L.; Liu, Y.; Xu, G.; Wang, T.; Cheng, H.; Wang, Z.; Zhang, X.; Wei, H.; George, C.; Mellouki, A.; Herrmann, H.; Wang, L.; Chen, J.; Ji, M.; Zhang, L.; Francisco, J. S. Imaging of pH distribution inside individual microdroplet by stimulated Raman microscopy. *Proc. Natl. Acad. Sci. U.S.A.* **2023**, *120* (20), No. e2219588120.
(70) Heine, N.; Houle, F. A.; Wilson, K. R. Connecting the Elementary Reaction Pathways of Criegee Intermediates to the Chemical Erosion of Squalene Interfaces during Ozonolysis. *Environ. Sci. Technol.* **2017**, *51* (23), 13740−13748.

https://doi.org/10.1021/acsestair.5c00189
ACS EST Air 2025, 2, 2491−2503